Acta Mech Sin (2009) 25:517–527
DOI 10.1007/s10409-009-0239-5

RESEARCH PAPER

A novel mesh-free poly-cell Galerkin method

C. Zheng · X. H. Tang · J. H. Zhang · S. C. Wu

Received: 10 March 2008 / Revised: 17 November 2008 / Accepted: 10 December 2008 / Published online: 4 March 2009

Abstract A novel numerical method is explored and named as mesh-free poly-cell Galerkin method. An improved moving least-square (MLS) scheme is presented, which can avoid the matrix inversion in standard MLS and can be used to construct shape functions possessing delta Kronecher property. A new type of local support is introduced to ensure the alignment of integral domains with the cells of the background mesh, which will reduce the difficult in integration. An intensive numerical study is conducted to test the accuracy of the present method. It is observed that solutions with good accuracy can be obtained with the present method.

Keywords MPG · CO-MSL · Mesh-free · Meshless · Voronoi diagram

1 Introduction

In the finite element method (FEM), the geometrical boundaries have to present as mesh lines [1,2]. Therefore, the mesh is difficult to generate if the geometrical boundaries are very complex or changing with time. To avoid the inconvenience of FEM, the so called mesh-free methods have been developed, both for structural [3–6] and fluid mechanics problems [7–9]. These new methods use the idea of a polynomial interpolant that fits a number of points minimizing the distance between the interpolated function and the value of the unknown points [10]. Many approaches of mesh-free methods have achieved significant progress in recent years. They include the smoothed hydrodynamic method (SPH) [11], the element-free Galerkin method (EFG) [12], the natural element method (NEM) [13], the reproducing kernel particle method (RKPM) [14,15], meshless finite element method (MFEM) [8], the meshless local Petrov–Galerkin method (MLPG) [16,17], and the linear conforming point interpolant method (LC-PIM) [18,19], etc.

Although so many approaches have been well-developed, there are still several common problems not completely solved. One of these problems, and perhaps the most important unsolved issue, is how to perform integral efficiently and precisely [20].

Gaussian integration is commonly used in Galerkin mesh-free methods for evaluating the stiffness matrix [21], and a background mesh is needed in the Gaussian integration. However, the local supports may not align with the integration cells. This misalignment is primarily responsible for the deterioration of accuracy and loss of convergence. Due to the complexity involved in standard Gaussian integration, two new mesh-free methods are explored by Atluri and his colleagues [22]. The first is called local boundary integral equation (LBIE) method and the second is called local Petrove-Galerkin (MLPG) method. Both use a local-Galerkin weak form in order to avoid the need for a background mesh and integrations are performed on subdomains surrounding the nodes. However, these local integrations will result in an unsymmetrical general stiffness matrix. Besides Gaussian integration techniques, another class of

C. Zheng (✉) · X. H. Tang · J. H. Zhang
State Key Laboratory of Hydraulics and Mountain River Engineering, Sichuan University, 610065 Chengdu, China
e-mail: C.Zheng85@gmail.com

S. C. Wu
State Key Laboratory of Digital Manufacturing and Equipment Technology, Huazhong University of Science and Technology, 430074 Wuhan, China

S. C. Wu
Centre for Advanced Computations in Engineering Science (ACES), Department of Mechanical Engineering,
National University of Singapore, Singapore 117576, Singapore

quadrature approaches is the stabilized nodal integration methods [23,24]. However, the nodal volumes used in nodal integration are still hard to evaluate. Although the Voronoi diagram is used to compute nodal volumes [25,26], deterioration of accuracy is still caused by the complexity of integral domains.

Besides the problem of integration, another problem of the mesh-free method is the imposition of essential boundary conditions, due to the lack of the delta Kronecher property ($\varphi_i(X_j) = \delta_{ij}$). This is the immediate consequence, in the referred mesh-free methods, of using approximation functions instead of interpolation functions.

In addition to the two problems mentioned above, there are some other problems including how to assign the radius of the support domain which influences the result greatly, how to find connective nodes efficiently, etc.

A new numerical approach named Poly-cell Galerkin Method (MPG) is explored in this paper, in which schemes of solving the above mentioned problems are proposed. The scheme of MPG is as follows.

First, the orthonormalized-moving least square (O-MLS) method is presented, in which, the basis functions such as $(1,\ x,\ y,\ z,\ xy,\ yz,\ xz,\ x^2,\ y^2,\ z^2)$ are orthonormalized. O-MLS avoid computation of matrix inversion and shape functions can be obtained even if the number of nodes is very small or some of the nodes are co-linear. Thereafter, the constrained orthonormalized-moving least square (CO-MLS) method is presented to construct shape functions that possess the delta Kronecher property. Therefore, imposition of essential boundary conditions becomes simple in MPG.

In standard mesh-free methods, the local support is a circle or a rectangular. These forms of local support make the mesh-free methods more flexible than FEM, however, they also causes the integration of stiffness matrix more difficult. The idea of poly-cell local support is explored here, which can avoid the error caused by integral boundaries in evaluating stiffness matrix. This poly-cell local support can be used over any background mesh, and the widely used Voronoi diagram is adopted in this paper.

The outline of this paper is as follows: The O-MLS is presented in Sect. 2 and the CO-MLS is presented in Sect. 3. Section 4 shows how to obtain the poly-cell local support and how to construct shape functions with the poly-cell local support. Some numerical examples are studied in Sect. 5 and some conclusions are discussed in Sect. 6.

2 Orthonormalized: moving least-square approximation

The moving least-square (MLS) method is now a commonly used alternative for constructing shape functions in most of meshfree methods proposed so far. Two excellent features make it more popular than other interpolant scheme: (1) the approximated field is continuous and smooth over the entire problem domain; and (2) it is capable of producing an approximation in desired order of consistency and compatibility. Unfortunately, the *moment matrix* inversion is always required, and the inverse of this matrix does not exist when the number of nodes is small or the nodes scatter collinearly in some special cases. By orthonormalizing basis functions, an Orthonormalized—moving least-square approximation is formulated to overcome above inherent drawbacks.

2.1 Briefing the moving least-square

Consider a field $u(\boldsymbol{x})$ defined in the 2D domain Ω with boundary Γ, which can be approximated over the poly-cell local support in the following form

$$u(\boldsymbol{x}) \approx u^h(\boldsymbol{x}) = \sum_{i=1}^{m} a_i(\boldsymbol{x}) p_i(\boldsymbol{x}) = \boldsymbol{a}^{\mathrm{T}}(\boldsymbol{x})\boldsymbol{p}(\boldsymbol{x}), \tag{1}$$

where $\boldsymbol{p}(\boldsymbol{x})$ is a vector of basis functions built by the Pascal's triangles, $\boldsymbol{a}(\boldsymbol{x})^{\mathrm{T}} = \{a_1(\boldsymbol{x}), a_2(\boldsymbol{x}), \ldots, a_m(\boldsymbol{x})\}$ is a vector of unknown parameters that depends on $\boldsymbol{x}^{\mathrm{T}} = [x, y]$, and m is the number of basis functions. For two dimensions, basis function $\boldsymbol{p}(x)$ of order 1 and 2 is written, respectively, by

$$\begin{aligned} \boldsymbol{p}^{\mathrm{T}}(\boldsymbol{x}) &= \{p_1(\boldsymbol{x}) \quad p_2(\boldsymbol{x}) \quad p_3(\boldsymbol{x})\} = \{1 \quad x \quad y\}, \\ m &= 3, \end{aligned} \tag{2}$$

$$\begin{aligned} \boldsymbol{p}^{\mathrm{T}}(\boldsymbol{x}) &= \{p_1(\boldsymbol{x}) \quad p_2(\boldsymbol{x}) \ldots \quad p_6(\boldsymbol{x})\} \\ &= 1\{x \quad y \quad xy \quad x^2 \quad y^2\}, \quad m = 6, \end{aligned} \tag{3}$$

where m is the number of monomial terms.

Note that the coefficient $a_i(\boldsymbol{x})$ is an arbitrary function of interested node $\boldsymbol{x}$, and m is usually much smaller than n. To determine $\boldsymbol{a}(\boldsymbol{x})$, a quadratic functional $I(\boldsymbol{x})$ is constructed using the approximated values of field function $u^h(\boldsymbol{x})$ and the nodal parameters, $u_i = u(\boldsymbol{x}_i)$ as

$$I(\boldsymbol{x}) = \sum_{i=1}^{n} \left[w_i \left(\boldsymbol{a}^{\mathrm{T}}(\boldsymbol{x})\boldsymbol{p}(\boldsymbol{x}) - u_i \right)^2 \right], \tag{4}$$

in which w_i is a weight function and n the number of supporting nodes. The stationarity of I with respect to $\boldsymbol{a}(x)$ leads to the following linear equation system:

$$\boldsymbol{a}(\boldsymbol{x}) = \boldsymbol{A}^{-1}(\boldsymbol{x})\boldsymbol{B}(\boldsymbol{x})\boldsymbol{u}, \tag{5}$$

where the moment matrix $\boldsymbol{A}$ and basis matrix $\boldsymbol{B}$ are expressed, respectively,

$$\begin{aligned} \boldsymbol{A}(\boldsymbol{x}) &= \sum_{i=1}^{n} w_i(\boldsymbol{x})\boldsymbol{p}(\boldsymbol{x}_i)\boldsymbol{p}^{\mathrm{T}}(\boldsymbol{x}_i), \\ w_i(\boldsymbol{x}) &\equiv w(\boldsymbol{x} - \boldsymbol{x}_i), \end{aligned} \tag{6}$$

$$\boldsymbol{B}(x) = [w_1(\boldsymbol{x})\boldsymbol{p}(\boldsymbol{x}_1) \quad w_2(\boldsymbol{x})\boldsymbol{p}(\boldsymbol{x}_2) \ \ldots \ w_n(\boldsymbol{x})\boldsymbol{p}(\boldsymbol{x}_n) \tag{7}$$

$$\boldsymbol{u} = (u_1, u_2, \ldots, u_n)^{\mathrm{T}}. \tag{8}$$

Substituting Eq. 5 back into Eq. 1 leads to

$$u^h(x) = \sum_{i=1}^{n} \varphi_i u_i = \boldsymbol{\Phi}^{\mathrm{T}}\boldsymbol{u} \tag{9}$$

and

$$\begin{aligned}\boldsymbol{\Phi}^{\mathrm{T}}(\boldsymbol{x}) &= \boldsymbol{p}^{\mathrm{T}}(\boldsymbol{x})\boldsymbol{A}^{-1}(\boldsymbol{x})\boldsymbol{B}(\boldsymbol{x}) \\ &= \{\varphi_1(\boldsymbol{x}) \quad \varphi_2(\boldsymbol{x}) \quad \ldots \quad \varphi_n(\boldsymbol{x})\}\end{aligned} \tag{10}$$

is the vector of the MLS shape functions.

The derivative of shape function $\boldsymbol{\Phi}$ is given as

$$\begin{aligned}\boldsymbol{\Phi}^{\mathrm{T}}_{,x}(\boldsymbol{x}) = \boldsymbol{p}^{\mathrm{T}}_{,x} \cdot \boldsymbol{A}^{-1} \cdot \boldsymbol{B} + \boldsymbol{p}^{\mathrm{T}} \cdot (\boldsymbol{A}^{-1})_{,x} \cdot \boldsymbol{B} \\ + \boldsymbol{p}^{\mathrm{T}} \cdot \boldsymbol{A}^{-1} \cdot \boldsymbol{B}_{,x},\end{aligned} \tag{11}$$

where a comma designates a partial derivative with respect to the indicated spatial variable $\boldsymbol{x}$.

It can be clearly seen that the inversion of moment matrix $\boldsymbol{A}$ have to be performed frequently in both Eqs. 14 and 15. Only the requirement of $n \gg m$ is satisfied can prevent the singularity of the weighted moment matrix $\boldsymbol{A}$. Importantly, it is very probable that the inversion of $\boldsymbol{A}$ does not exist especially for the special case of arbitrarily distributed nodes in the local circle support of interested node. On the other hand, the frequent operation of matrix inversion usually results in the computational expensive cost. It is therefore, necessary to pursue some kind of special technique to avoid the frequent inversion operation of moment matrix $\boldsymbol{A}$ in the presence of higher order smoothness of the MLS shape functions.

2.2 Orthonormalized moving least square

An Orthonormalized moving least-square (O-MLS) approximation is formulated in details by orthonormalizing the basis functions $\boldsymbol{p}$ utilized in the conventional MLS. This scheme not only can ensure existence of the inversion of coefficient matrix but extend our mind to connect different approximation scheme used in meshfree methods.

First, define a symbol operator as

$$(f(\boldsymbol{x}), g(\boldsymbol{x}))_w = \sum_{i=1}^{n} w_i f(\boldsymbol{x}_i) g(\boldsymbol{x}_i), \tag{12}$$

where f and g can be arbitrary variables, n is the number of supporting nodes, $\boldsymbol{x}_i$ denotes the coordinates of node i, and w is the weight function same to MLS.

2.2.1 Orthogonalizing vector $\boldsymbol{p}$

Vector $\boldsymbol{p}$ can be orthogonalized as follows

$$\boldsymbol{s} = \{s_1, s_2, \ldots, s_m\}^{\mathrm{T}} = \boldsymbol{V}\boldsymbol{p}, \tag{13}$$

where $\boldsymbol{V}$ is an orthogonalizing matrix with dimension of $m \times m$. Assume V_{ij} is the elementary of matrix $\boldsymbol{V}$ in line i and column j, and then V_{ij} can be computed by

$$\begin{aligned}V_{ij} = \begin{cases} 0, & \text{if } i < j, \\ 1, & \text{if } i = j \\ -\sum_{k=j}^{i-1} \frac{(p_i, s_k)_w}{(s_k, s_k)_w} V_{kj}, & \text{if } i > j, \end{cases} \\ i, j = 1, 2, \ldots, m.\end{aligned} \tag{14}$$

The proof of Eq. 18 by the Smith orthogonalizing formulas is given as below. The Smith orthogonalizing formulas are [27]

$$s_1 = p_1, \tag{15}$$

$$s_2 = p_2 - \frac{(p_2, s_1)_w}{(s_1, s_1)_w} \times s_1, \tag{16}$$

$$\ldots$$

$$s_i = p_i - \sum_{k=1}^{i-1} \frac{(p_i, s_k)_w}{(s_k, s_k)_w} \times s_k. \tag{17}$$

Substituting Eq. 17 into Eq. 21 yields

$$s_i = p_i - \sum_{k=1}^{i-1} \sum_{j=1}^{m} \frac{(p_i, s_k)_w}{(s_k, s_k)_w} \times V_{kj} s_j, \tag{18}$$

in which s_i is computed with $p_1, p_2, \ldots, p_i$. Note that when $j > k$, $V_{kj} = 0$, hence

$$s_i = p_i - \sum_{k=1}^{i-1} \sum_{j=1}^{k} \frac{(p_i, s_k)_w}{(s_k, s_k)_w} \times V_{kj} p_j, \tag{19}$$

$$s_i = p_i - \sum_{j=1}^{i-1} \left(\sum_{k=j}^{i-1} \frac{(p_i, s_k)_w}{(s_k, s_k)_w} \times V_{kj} \right) p_j. \tag{20}$$

Expressing Eq. 24 in the matrix form and then Eq. 18 can be obtained.

2.2.2 Normalizing vector $\boldsymbol{s}$

Normalizing the vector $\boldsymbol{s}$ yields

$$\boldsymbol{r}(\boldsymbol{x}) = \{r_1(\boldsymbol{x}) \quad r_2(\boldsymbol{x}) \quad \ldots \quad r_m(\boldsymbol{x})\}^{\mathrm{T}}, \tag{21}$$

$$r_i = \frac{s_i}{\sqrt{(s_i, s_i)_w}}, \quad i = 1, 2, \ldots, m. \tag{22}$$

Substituting Eq. 13 into Eq. 17 yields

$$\boldsymbol{r} = \boldsymbol{H}\boldsymbol{p}, \tag{23}$$

where $\boldsymbol{H}$ is an orthonormalizing matrix with dimension

$m \times m$. Suppose H_{ij} is the elementary of matrix $\boldsymbol{H}$ in line i and column j, and then H_{ij} can be computed by

$$H_{ij} = \frac{V_{ij}}{\sqrt{(s_i, s_i)_w}}, \quad i, j = 1, 2, \ldots, m. \tag{24}$$

2.2.3 Computing shape functions $\boldsymbol{\Phi}$

Now use the vector $\boldsymbol{r}$ as the basis vector and substitute $\boldsymbol{r}$ as $\boldsymbol{p}$ into Eq. 1 of standard MLS. A similar form of shape functions will be obtained as follows

$$\boldsymbol{\Phi}^{\mathrm{T}} = \boldsymbol{r}^{\mathrm{T}}(\boldsymbol{x})\boldsymbol{A}^{-1}\boldsymbol{B}, \tag{25}$$

$$\boldsymbol{A}(\boldsymbol{x}) = \sum_{i=1}^{n} w_i(\boldsymbol{x})\boldsymbol{r}(\boldsymbol{x}_i)\boldsymbol{r}^{\mathrm{T}}(\boldsymbol{x}_i), \tag{26}$$

$$\boldsymbol{B}(x) = [w_1(\boldsymbol{x})\boldsymbol{r}(\boldsymbol{x}_1) \quad w_2(\boldsymbol{x})\boldsymbol{r}(\boldsymbol{x}_2) \quad \ldots \quad w_n(\boldsymbol{x})\boldsymbol{r}(\boldsymbol{x}_n)] \tag{27}$$

Since the vector $\boldsymbol{r}$ is an orthonormalized vector, matrix $\boldsymbol{A}$ will be an identical matrix, and then

$$\boldsymbol{\Phi}^{\mathrm{T}} = \boldsymbol{r}^{\mathrm{T}}(\boldsymbol{x})\boldsymbol{B}. \tag{28}$$

The partial derivative of shape function $\boldsymbol{\Phi}$ can be easily obtained as

$$\boldsymbol{\Phi}^{\mathrm{T}}_{,x} = \boldsymbol{r}^{\mathrm{T}}_{,x}\boldsymbol{B} + \boldsymbol{r}^{T}\boldsymbol{B}_{,x}. \tag{29}$$

Compared with classical MLS, the O-MLS is conducted without any inversion of matrix. This feature makes the O-MLS more suitable to irregular node distribution in the shape function construction of meshfree methods. This advantage also implies the MPG very robust in simulating problems of cracks and complex geometries, which are intensively studied in the following analysis of cracks. More importantly, the O-MLS permits one select any number of nodes in the nodal support domain. When $n > m$, the O-MLS is referred to as the standard MLS; and when $n \leq m$, it can still be performed without any problems. This flexibility of selecting nodes indicates that fewer nodes can be used for interpolation and integration, which optimizes the computation cost and numerical accuracy.

3 Constrained orthonormalized-moving least square (CO-MSL) method

Based on O-MLS, the CO-MLS technique is presented, which can be used to construct shape functions that posses delta Kronecher property.

3.1 Constrained by one node

Same to O-MLS, $\boldsymbol{r}$ is selected as the basis functions. The approximation function is expressed as follows.

$$u(\boldsymbol{x}) \approx u^h(\boldsymbol{x}) = \sum_{i=1}^{m} a_i(\boldsymbol{x})r_i(\boldsymbol{x}) = \boldsymbol{a}^{\mathrm{T}}(\boldsymbol{x})\boldsymbol{r}(\boldsymbol{x}). \tag{30}$$

Assume the shape function must satisfy the condition as follows.

$$u^h(\boldsymbol{x}_q) = \boldsymbol{a}^{\mathrm{T}}(\boldsymbol{x}_q)\boldsymbol{r}(\boldsymbol{x}_q) = u_q, \tag{31}$$

in which q is one of the supporting nodes. According to Lagrange multiplier method, construct function J as follows:

$$J = I + 2\lambda(\boldsymbol{a}^{\mathrm{T}}\boldsymbol{r}(\boldsymbol{x}_q) - u_q). \tag{32}$$

The stationarity of J with respect to $\boldsymbol{a}$ leads to the following linear equation system.

$$a_i = (\boldsymbol{r}_i, \boldsymbol{u})_w - \lambda r_{iq}, \tag{33}$$

in which r_{iq} represents the value of r_i at node q. Substituting Eq. 33 into Eq. 31 yields,

$$\begin{aligned}\lambda &= \frac{\sum_{i=1}^{m}[r_{iq} \cdot (\boldsymbol{r}_i, \boldsymbol{u})_w] - u_q}{\sum_{i=1}^{m} r_{iq}^2} \\ &= \frac{\sum_{j=1}^{n}\left[\left(\sum_{i=1}^{m} w_j r_{iq} r_{ij}\right) u_j\right] - u_q}{\sum_{i=1}^{m} r_{iq}^2}.\end{aligned} \tag{34}$$

Equation 34 can be expressed as follows,

$$\lambda = \sum_{j=1}^{n} f_j^{[q]} u_j, \tag{35}$$

where

$$f_j^{[q]} = \begin{cases} \dfrac{\sum_{i=1}^{m}(w_j R_{iq} R_{ij})}{\sum_{i=1}^{m} R_{iq}^2}, & \text{if } j \neq q, \\ \dfrac{\sum_{i=1}^{m}(w_j R_{iq} R_{ij}) - 1}{\sum_{i=1}^{m} R_{iq}^2}, & \text{if } j = q, \end{cases}$$
$$j = 1, 2, \ldots, n. \tag{36}$$

Substituting Eq. 35 into Eq. 33 yields,

$$a_i = \sum_{j=1}^{n}(w_j r_{ij} - f_j^{[q]} r_{iq}) u_j, \quad i = 1, 2, \ldots, m. \tag{37}$$

Substituting Eq. 37 into Eq. 30 yields,

$$\boldsymbol{\Phi}^{\mathrm{T}} = \boldsymbol{r}^{\mathrm{T}}(\boldsymbol{x})\boldsymbol{B}^{[q]}, \tag{38}$$

$$\boldsymbol{B}^{[q]} = \{\boldsymbol{B}_1^{[1]}, \boldsymbol{B}_2^{[1]}, \cdots, \boldsymbol{B}_n^{[1]}\}, \tag{39}$$

$$\boldsymbol{B}_j^{[q]} = w_j \boldsymbol{r}(\boldsymbol{x}_j) - f_j^{[q]} \boldsymbol{r}(\boldsymbol{x}_q),$$
$$i = 1, 2, \ldots, m; \; j = 1, 2, \ldots, n. \tag{40}$$

3.2 Formulas of CO-MLS

$\boldsymbol{B}^{[q]}$ includes the constrained condition of node q. If constrained conditions of all nodes are considered, a modification on matrix $\boldsymbol{B}$ should be made as follows.

$$\boldsymbol{B}'_j = \sum_{q=1}^{n} w'_j \boldsymbol{B}_j^{[q]}, \tag{41}$$

where w'_q is called constraining weight function of node q. w'_q should satisfy relations as bellow.

$$\sum_{q=1}^{n} w'_q = 1 \tag{42}$$

$$w'_q(\boldsymbol{x}_i) = \begin{cases} 1, \text{ if } q = i, \\ 0, \text{ if } q \neq i. \end{cases} \tag{43}$$

The shape functions of CO-MLS can be expressed as

$$\boldsymbol{\Phi}^{\mathrm{T}} = \boldsymbol{r}^{\mathrm{T}}(\boldsymbol{x})\boldsymbol{B}', \tag{44}$$

$$\boldsymbol{B}' = \{\boldsymbol{B}'_1, \boldsymbol{B}'_2, \ldots, \boldsymbol{B}'_n\}, \tag{45}$$

$$\boldsymbol{B}'_j = w_j \boldsymbol{r}_j - \sum_{q=1}^{n} w'_q f_j^{[q]} \boldsymbol{r}(\boldsymbol{x}_q). \tag{46}$$

4 Poly-cell local support domain and Galerkin weak form

4.1 Poly-cell local support domain

In the FEM, the geometrical boundaries such as outlines or cracks, have to present as mesh lines. If an crack is located in elements, as shown in Fig. 1, it would be hard to deal with. Figure 1 also shows that an crack located in a model of mesh-free methods. It is found that the mesh-free methods are more flexible in dealing with the geometrical boundaries. For most of mesh-free methods, circular loacal support are adopted. A simple model and the circular local supports of each node are plotted in Fig. 2. It is obvious that the circular local support causes serious difficulty in evaluating the stiffness matrix. Thus we try to find a type of local support, which is easy to evaluate the stiffness matrix and can still deal with the geometrical boundaries in the same way as traditional mesh-free methods. The Poly-cell local support domain is then explored to solve this problem. A background mesh is needed in poly-cell local support domain. The background mesh can be arbitrary mesh consisting polygons in 2D space or polyhedrons in 3D space. There are many ways to generate the background mesh for poly-cell local support, and the Voronoi diagram is an easy way. The Voronoi diagram is a partition of the problem domain Ω into non-overlapping convex subdomains Ω_i called Voronoi cell. Each Voronoi cell is associated with a node I and any point in Ω_i is closer to I than to any other node [8]. A Voronoi diagram is shown in Fig. 3.

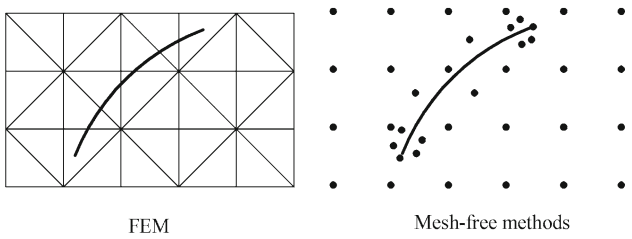

Fig. 1 Illustration of a crack, noting that the mesh-free method is easy to deal with discontinuity

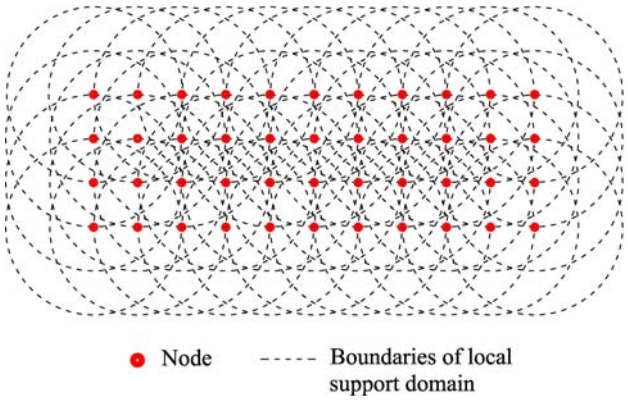

Fig. 2 Inllustration of circular local support, noting that accurate integration is hard to perform

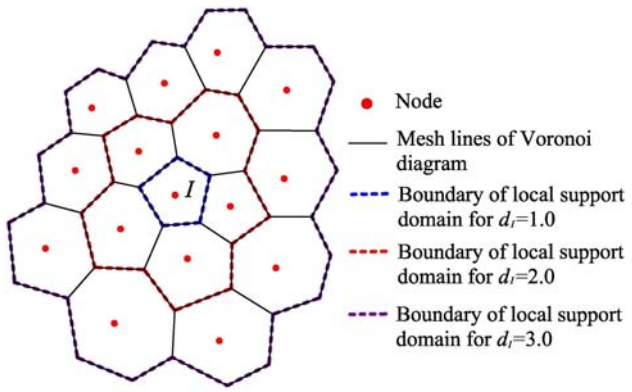

Fig. 3 Poly-cell local support based on Voronoi diagram

On the background mesh, each node influences several nearby cells, and like the FEM, the integration can be completed by looping for cells. The poly-cell local support with different influence-degree d_I can be obtained as shown in Fig. 3. In CO-MLS, each node has a weak supporting domain in which $w > 0$ and a strong supporting in which $w' > 0$ in. Denote d_I^{w} as the influence-degree of the weak supporting and d_I^{s} as the influence-degree of the strong supporting domain. Obviously, these two parameter play an important role for efficiency. In order to obtain high effieciency in com-

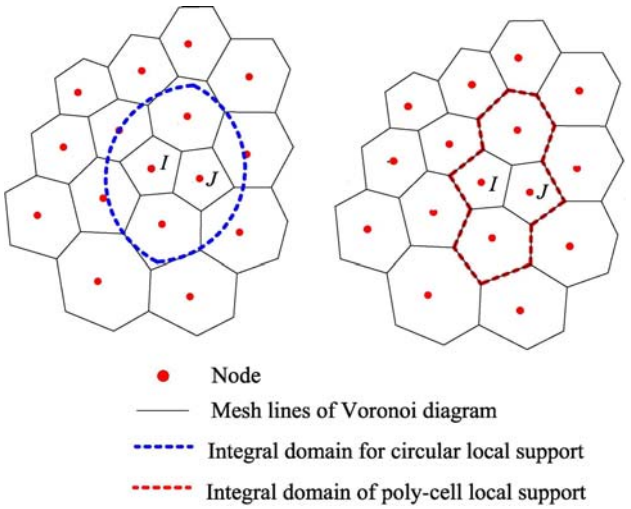

Fig. 4 Comparison of integral domain

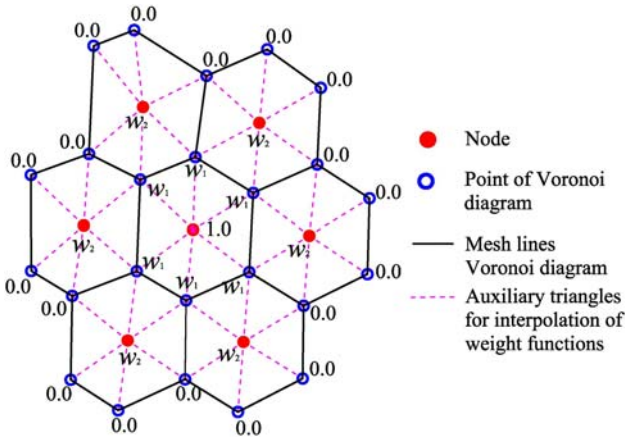

Fig. 5 Illustration of interpolated weight functions

putation, d_I^{w} is evaluated 2.0 and d_I^{s} is evaluated 1.0, which are the smallest values that ensure the overlapping of local support. The cell Ω_I and all of its neighbor cells are the weak supporting cells of node I. Only Ω_I is the strong support cell of node I. Figure 4 shows the integral domain of stiffness between node I and J, for both circular local support and poly-cell local support. It is obvious that if the integration is performed by looping for the cells, the poly-cell local support will achieved better accuracy than the circular local support.

4.2 Weight functions

It is a difficult matter to construct the weight functions on a poly-cell local support domain because its edges is more complex than a circular domain. An interpolated weight functions is introduced here.

For the node I, the computation of the interpolated weight functions is shown in Fig. 5. Auxiliary triangulations are generated and the weight functions on the vertices of these triangles are assigned. The weight functions on the local support domain are obtained by interpolation on these triangulations. In the numerical experiments of this paper, for the weight functions, w_1 is assigned 2/3 and w_2 is assigned 1/3, and for the constraining weight functions, w_1 is assigned 0 and w_2 is assigned 0.

A weight function, a constraining weight function and a shape function are plotted in Figs. 6a, b and c, respectively. The figure reveals that the shape functions are C^∞ in the auxiliary triangles and are C^0 on the edges of the auxiliary triangles. The delta Kronecher property of the shape functions is also manifested by the figure.

4.3 Galerkin weak form

Since the MPG is based on Galerkin weak form, the methodoly of Galerkin weak form will be reviewed in this section. Consider a solid problem defined in domain Ω bounded by $\Gamma(\Gamma = \Gamma_t + \Gamma_u)$, the governing equations of these problems can be expressed as follows [1]:

Equilibrium equation:

$$\boldsymbol{L}^{\mathrm{T}}\boldsymbol{\sigma} + \boldsymbol{b} = 0, \quad \text{in } \Omega. \tag{47}$$

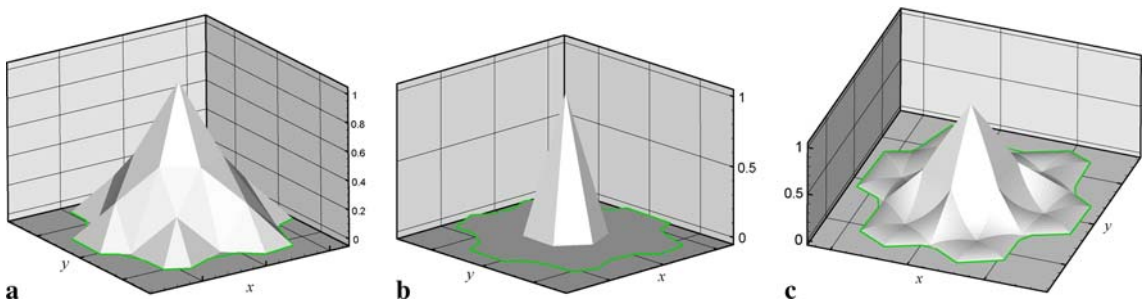

Fig. 6 Shape function of poly-cell local support based on Voronoi diagram. **a** Weight function of node I; **b** Constraining weight function of node I; **c** Shape function

Natural and essential boundary conditions:

$$\begin{aligned} &\boldsymbol{\sigma}\cdot\boldsymbol{n}=\bar{\boldsymbol{t}}, \quad \text{in} \quad \Gamma_t,\\ &\boldsymbol{u}=\bar{\boldsymbol{u}}, \quad \text{in} \quad \Gamma_u, \end{aligned} \tag{48}$$

where $\boldsymbol{L}=\begin{bmatrix} \frac{\partial}{\partial x} & 0 & \frac{\partial}{\partial y} \\ 0 & \frac{\partial}{\partial y} & \frac{\partial}{\partial x} \end{bmatrix}^{\mathrm{T}}$ is the differential operator; $\boldsymbol{\sigma}=[\sigma_x,\sigma_y,\sigma_{xy}]^{\mathrm{T}}$ is the stress vector, $\boldsymbol{u}=[u,v,w]$ is the displacement vector, $\boldsymbol{b}=[b_x,b_y]^{\mathrm{T}}$ is the body force vector, $\bar{\boldsymbol{t}}$ is the prescribed traction on natural boundaries, $\bar{\boldsymbol{u}}$ is the prescribed displacement on essential boundaries, and $\boldsymbol{n}$ is the vector of unit outward normal at a point on the natural boundary.

The unconstrained Galerkin weak form is presented as follows:

$$\int_{\Omega}(\boldsymbol{L}\delta\boldsymbol{u})^{\mathrm{T}}\boldsymbol{D}\boldsymbol{L}\boldsymbol{u}\mathrm{d}\Omega-\int_{\Omega}\delta\boldsymbol{u}^{\mathrm{T}}\boldsymbol{b}\mathrm{d}\Omega -\int_{\Gamma_t}\delta\boldsymbol{u}^{\mathrm{T}}\boldsymbol{t}\mathrm{d}\Gamma=0. \tag{49}$$

For linear elasticity, the material matrix $\boldsymbol{D}$ is expressed as follows:

$$\boldsymbol{D}=\frac{E}{1-v^2}\begin{bmatrix} 1 & v & 0 \\ v & 1 & 0 \\ 0 & 0 & \frac{1-v}{2} \end{bmatrix} \tag{50}$$

for plane stress problem,

$$\boldsymbol{D}=\frac{E(1-v)}{(1+v)(1-2v)}\begin{bmatrix} 1 & \frac{v}{1-v} & 0 \\ \frac{v}{1-v} & 1 & 0 \\ 0 & 0 & \frac{1-2v}{2(1-v)} \end{bmatrix} \tag{51}$$

for plane strain problem, where E is Young's modules and v is possion's ratio.

Substituting the approximation equation into Galerkin weak form yields

$$\boldsymbol{K}\boldsymbol{u}=\boldsymbol{f}, \tag{52}$$

where

$$\boldsymbol{K}_{ij}=\int_{\Omega}\boldsymbol{B}_i^{\mathrm{T}}\boldsymbol{D}\boldsymbol{B}_j\mathrm{d}\Omega, \tag{53}$$

$$\boldsymbol{u}_i=\{u(\boldsymbol{x}_i),v(\boldsymbol{x}_i)\}^{\mathrm{T}}, \tag{54}$$

$$\boldsymbol{f}_i=\int_{\Gamma_t}\varphi_i^{\mathrm{T}}\bar{\boldsymbol{t}}\mathrm{d}\Gamma+\int_{\Omega}\varphi_i^{\mathrm{T}}\bar{\boldsymbol{b}}\mathrm{d}\Omega, \tag{55}$$

$$\boldsymbol{B}_i=\begin{bmatrix} \frac{\partial\varphi_i}{\partial x} & 0 & \frac{\partial\varphi_i}{\partial y} \\ 0 & \frac{\partial\varphi_i}{\partial y} & \frac{\partial\varphi_i}{\partial x} \end{bmatrix}^{\mathrm{T}}. \tag{56}$$

5 Numerical examples

An intensive numerical study for the present MPG is conducted in terms of the validation, accuracy and convergence using some benchmark examples. All the experiments is conducted on the numerical platform ASOF (analysis system of failure), which contains computer program of FEM, TFEM and most of mesh-free methods. The variable units used in the work are based on international standard unit system unless specially denoted.

To examine the accuracy and convergence, the relative L_2 error in displacement norm and in energy norm are defined as follows, respectively,

$$e_{\mathrm{d}}=\sqrt{\frac{\int_{\Omega}(\boldsymbol{u}^{\mathrm{exact}}-\boldsymbol{u}^{\mathrm{numerical}})^2\mathrm{d}\Omega}{\int_{\Omega}(\boldsymbol{u}^{\mathrm{exact}})^2\mathrm{d}\Omega}}, \tag{57}$$

$$e_{\mathrm{e}}=\sqrt{\frac{\frac{1}{2}\int_{\Omega}(\boldsymbol{\varepsilon}^{\mathrm{exact}}-\boldsymbol{\varepsilon}^{\mathrm{numerical}})^{\mathrm{T}}\boldsymbol{D}(\boldsymbol{\varepsilon}^{\mathrm{exact}}-\boldsymbol{\varepsilon}^{\mathrm{numerical}})\mathrm{d}\Omega}{\frac{1}{2}\int_{\Omega}(\boldsymbol{\varepsilon}^{\mathrm{exact}})^{\mathrm{T}}\boldsymbol{D}\boldsymbol{\varepsilon}^{\mathrm{exact}}\mathrm{d}\Omega}}, \tag{58}$$

where the superscript "exact" represents the exact or analytical solution and the "numerical" denotes a numerical solution obtained using a numerical technique including the present MPG. Each Voronoi cell is divided into several auxiliary triangles and for each triangle 3-point Hammer quadrature is utilized to evaluate the stiffness matrix.

5.1 Cantilever beam

A 2D cantilever beam with length L, height D and unit thickness is studied for the various behaviors of the TFEM as a benchmark problem. The beam is fixed at the left end and subjected to a parabolic traction P at the free end in Fig. 7. The analytical solutions of displacement and stress [28] for the plane stress case is given by,

$$u_x=-\frac{Py}{6EI}\left[(6L-3x)x+(2+v)\left(y^2-\frac{D^2}{4}\right)\right], \tag{59}$$

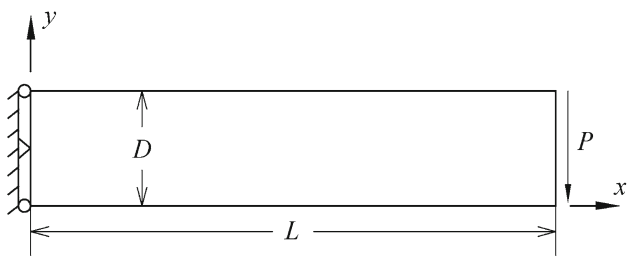

Fig. 7 A cantilever beam

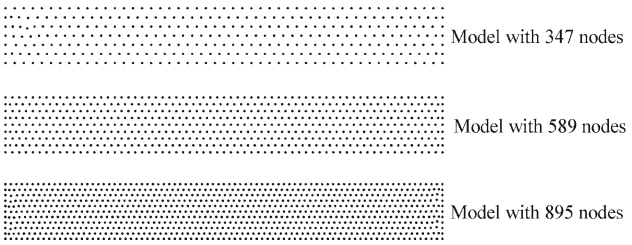

Fig. 8 Three models for the cantilever beam problem

$$u_y = \frac{P}{6EI}\left[3\nu\left(y-\frac{1}{2}D\right)^2(L-x)+\frac{1}{4}(4+5\nu)D^2x + (3L-x)x^2\right], \tag{60}$$

$$\sigma_{xx} = -\frac{P}{I}(L-x)\left(y-\frac{1}{2}D\right), \tag{61}$$

$$\sigma_{yy} = 0, \tag{62}$$

$$\sigma_{xy} = -\frac{Py}{2I}(y-D), \tag{63}$$

where I is the moment of inertia of $D^3/12$. For plane strain problem, Eqs. 59 and 60 hold after substituting E and ν with $E/(1-\nu^2)$ and $\nu/(1-\nu)$, respectively.

The parameters in the computation are taken as: $L = 8$, $D = 1$, $P = -1$, and $E = 3.0 \times 10^7$ unless specially denoted, and the plane strain conditions are assumed. In the computation, the nodes on the boundary of $x = 0$ are constrained using the exact displacements given from Eqs. 59 to 60, and the traction are specified on the boundary of $x = L$ using Eq. 63.

Three models are used (347, 589 and 895 nodes) to investigate the properties of the present method as shown in Fig. 8. To make a comparison, triangular element mesh was generated for each model and the numerical solutions of FEM are also given. The convergence curves are plotted in Fig. 9, for both TFEM and standard FEM. It is observed that the TFEM presents better accuracy than standard FEM.

To examine accuracy of the present method, the model with 895 nodes are sampled. The numerical solutions of deflection along the neutral line and the stress in the x direction along the line ($x = L/2$) of the beam are plotted in Fig. 10, together with analytical solutions. It is found the solutions of the present MPG agree with the analytical solutions very well and the accuracy of MPG is better than FEM.

5.2 An infinite plate with a hole

Figure 11a represents the infinite plate with a central hole subjected to a tensile traction P. Due to its symmetric, only the upper right quadrant of the plate is modeled with the dimensions of b in both x and y directions as shown in Fig. 11b. The analytical stress in the plate can be found in the polar coordinate [28].

$$\sigma_{xx} = P\left\{1-\frac{a^2}{r^2}\left[\frac{3}{2}\cos(2\theta)+\cos(4\theta)\right] + \frac{3a^4}{2r^4}\cos(4\theta)\right\}, \tag{64}$$

$$\sigma_{yy} = -P\left\{\frac{a^2}{r^2}\left[\frac{1}{2}\cos(2\theta)-\cos(4\theta)\right]+\frac{3a^4}{2r^4}\cos(4\theta)\right\}, \tag{65}$$

$$\sigma_{xy} = -P\left\{\frac{a^2}{r^2}\left[\frac{1}{2}\sin(2\theta)+\sin(4\theta)\right]-\frac{3a^4}{2r^4}\sin(4\theta)\right\}, \tag{66}$$

where θ is measured counterclockwise from the positive x-axis. Similarly, the analytical displacement of the plate is given as

$$u_r = \frac{P}{4\mu}\left\{r\left[\frac{\kappa-1}{2}+\cos(2\theta)\right]+\frac{a^2}{r}[1+(1+\kappa)\cos(2\theta)] - \frac{a^4}{r^3}\cos(2\theta)\right\}, \tag{67}$$

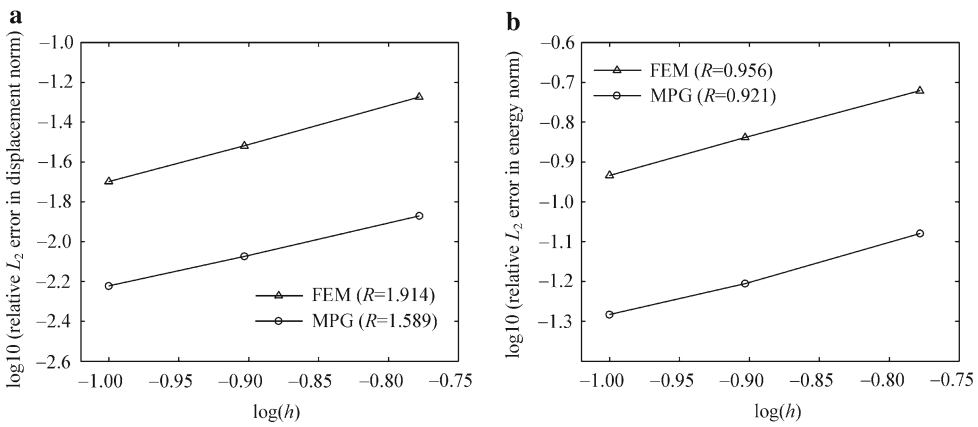

Fig. 9 Convergence of the cantilever beam. **a** Displacement norm; **b** energy norm

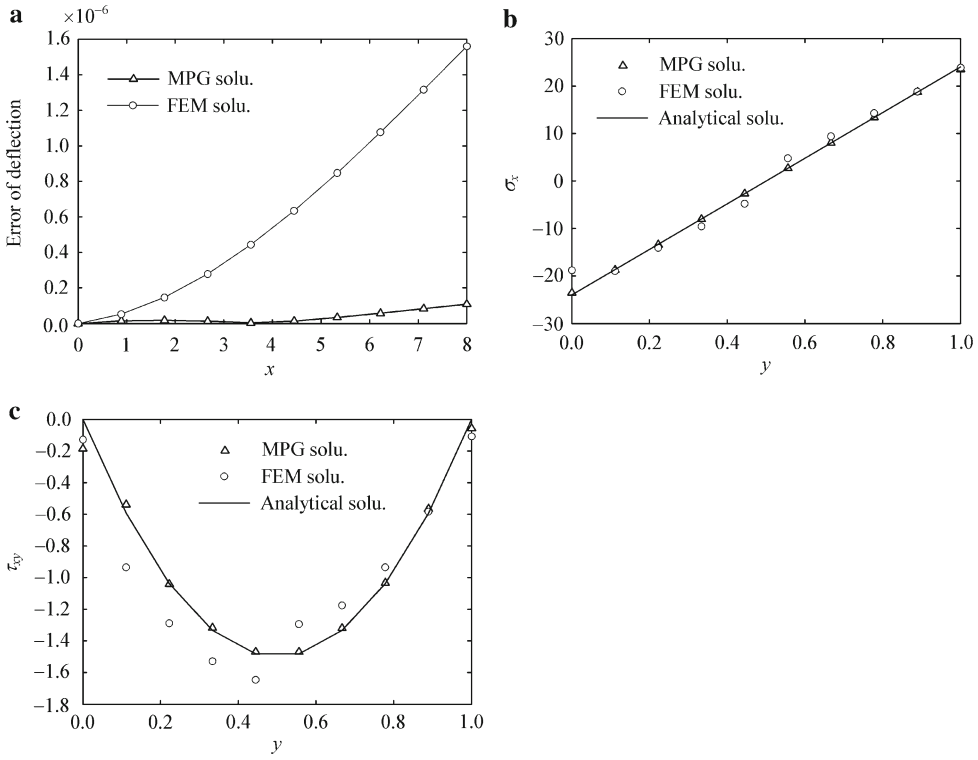

Fig. 10 Comparison of the solutions of the cantilever beam. **a** Error of deflection at neutral line; **b** σ_x at line $x = L/2$; **c** τ_{xy} at line $x = L/2$

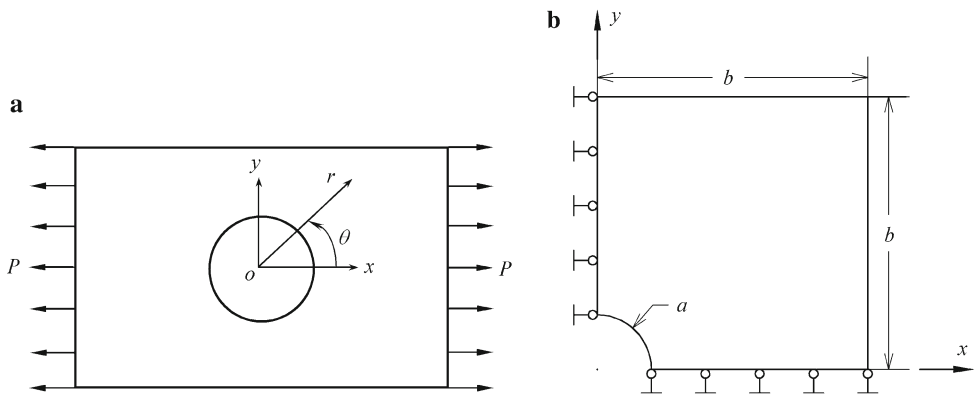

Fig. 11 An infinite plate with a hole. **a** Infinite plate with circular hole subjected to unidirectional tension; **b** domain sampling of the infinite plate

$$u_\theta = \frac{P}{4\mu}\left[(1-\kappa)\frac{a^2}{r} - r - \frac{a^4}{r^3}\right]\sin(2\theta), \tag{68}$$

where

$$\mu = \frac{E}{2(1+\nu)},$$

$$\kappa = \begin{cases} 3-4\nu, & \text{plane strain,} \\ \dfrac{3-\nu}{1+\nu}, & \text{plane stress.} \end{cases} \tag{69}$$

The parameters in this problem are taken as: $a = 1$, $b = 5$, $P = 1$, and plane stain state is assumed. The material used is linear elastic with Young's modules $E = 1.0 \times 10^3$ and Poisson's ratio $\upsilon = 0.25$ unless specially denoted. Analytical traction solutions are enforced on the boundaries at $x = 5.0$ and $y = 5.0$ and analytical displacement solutions are enforced on the remaining essential boundaries.

Three models are used (134, 278 and 474 nodes) to investigate the properties of the present method as shown in Fig. 12. To make a comparison, triangular element mesh was generated for each model and the numerical solutions of FEM are also given. The convergence curves are plotted in Fig. 13, for both TFEM and standard FEM. It is observed that the TFEM presents better accuracy than standard FEM.

To examine accuracy of the present method, the model with 134 nodes are sampled The numerical solutions at boundary line $x = 0$ and $y = 0$ of the plate are plotted in Fig. 14 and Fig. 15, respectively. It is found the solutions of the present MPG agree with the analytical solutions very

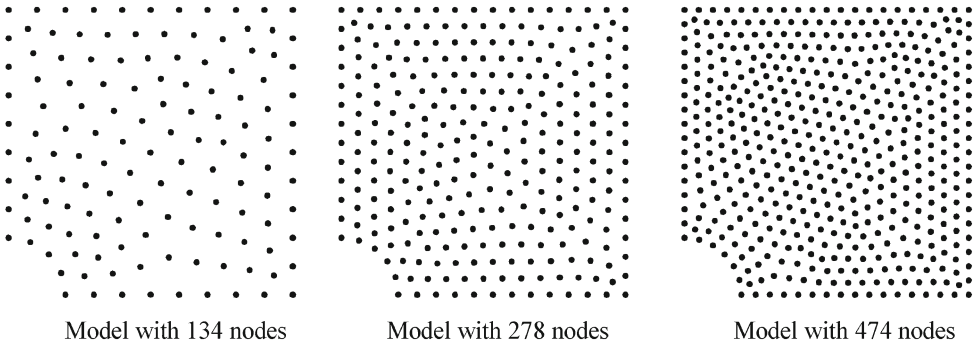

Fig. 12 Three models for the infinite plate with a hole

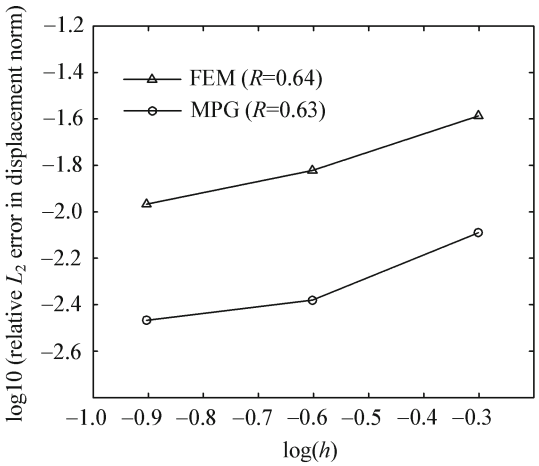

Fig. 13 Convergence of the infinite plate with a hole

well. The examples show that better accuracy can be achieved with the present MPG. Noting that even if the MPG just possess comparable accuracy with FEM, the MPG still has advantages because the MPG is more flexible than FEM in modeling practical problems with complex geometrical boundaries.

6 Conclusion

A MPG based on the voronoi diagram is presented in the paper. In the MPG, CO-MLS technique and the poly-cell local support domain are introduced firstly. An intensive numerical study is conducted to examine the accuracy of the present MPG. It is observed that good accuracy can be achieved with the MPG. The advantages of PGM are as follows.

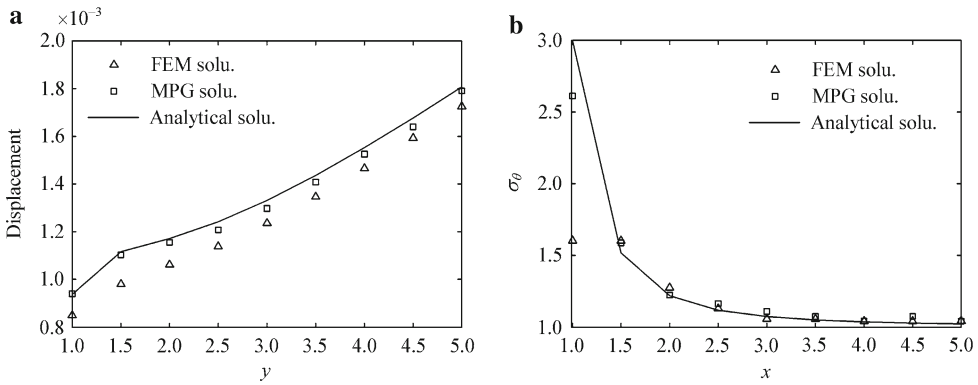

Fig. 14 Comparison of solutions at line $x = 0$. **a** Displacement; **b** stress in θ direction

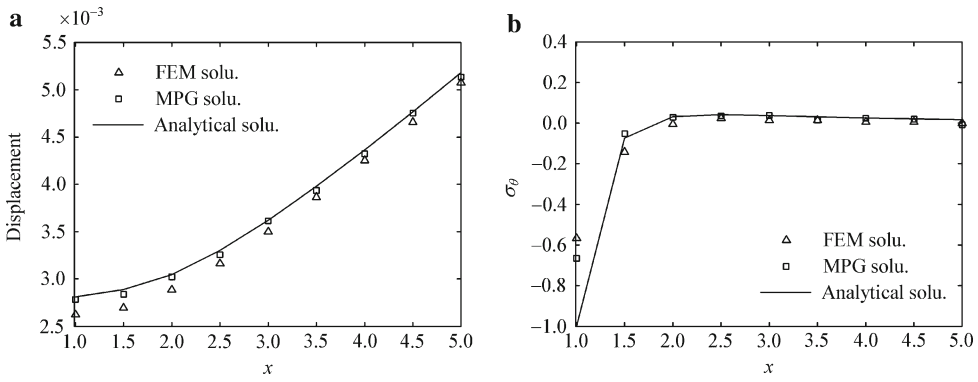

Fig. 15 Comparison of solutions at line $y = 0$. **a** Displacement; **b** Stress in θ direction

(1) Comparing with the methods based on circular support domain, the integration of PGM can be performed more efficiently and accurately. Furthermore, the assignment of radius of circular support domain greatly influence the results, however, the use of non-circular support domain avoid this assignment.
(2) Comparing with the FEM, the PGM is more flexible in dealing with the geometrical boundaries.
(3) The shape functions obtained by CO-MLS posses the Delta Kronecher property, so it is simple to impose essential boundary conditions. In addition, CO-MLS avoids the computation of matrix inversion, so it still works even if the number of nodes is very small or some of the nodes are co-line.
(4) Comparing with the non-Galerkin method, the general stiffness matrix is symmetric and positive definite.

References

1. Zienkiewicz, O.C., Cheung, Y.K.: The Finite Element Method in Continuum and Structural Mechanics, 3rd edn. McGraw Hill, New York (1967)
2. Zhang, J.H., He, J.D., Fan, J.W.: Static and dynamic stability assessment of slopes or dam foundations using a rigid body-spring element method. Int. J. Rock Mech. Mining Sci. **38**, 1081–1090 (2001)
3. Nayroles, B., Touzot, G., Villon, P.: Generalizing the finite element method: diffuse approximation and diffuse elements. Comput. Mech. **10**, 307–318 (2004)
4. Belytschko, T., Lu, Y.Y., Gu, L.: Crack propagation by element-free Galerkin methods. Eng. Fract. Mech. **51**, 295–315 (1995)
5. Han, Z., Yang, H.T., Liu, L.: Solving viscoelastic problems with cyclic symmetry via a precise algorithm and EFGM. Acta Mech. Sin. **22**, 170–176 (2006)
6. Guo, X.H., Fang, D.N., Soh, A.K., et al.: Analysis of piezoelectric ceramic multilayer actuators based on an electro-mechanical coupled meshless method. Acta Mech. Sin. **22**, 34–39 (2006)
7. Oñate, E., Idelsohn, S.R., Zienkiewicz, O.C., et al.: A stabilized finite point method for analysis of fluid mechanics problems. Comput. Methods Appl. Mech. Eng. **139**, 315–346 (1996)
8. Idelsohn, S.R., Oñate, E., Oñate, N., Pin, F.D.: The meshless finite element method. Int. J. Numer. Meth. Eng. **58**, 893–912 (2003)
9. Idelsohn, S.R., Oñate, E., Pin, F.D.: The particle finite element method: a powerful tool to solve incompressible flows with free-surfaces and breaking waves. Int. J. Numer. Meth. Eng. **61**, 964–989 (2004)
10. Idelsohn, S.R., Oñate, E.: To mesh or not to mesh. That is the question. Comput. Methods Appl. Mech. Eng. **195**, 4681–4696 (2006)
11. Monaghan, J.J.: Smoothed particle hydrodynamics. Ann. Rev. Astron. Astrophys. **30**, 543–574 (1992)
12. Belytschko, T., Lu, Y.Y., Gu, L.: Element free Garlerkin methods. Int. J. Numer. Meth. Eng. **37**, 229–256 (1994)
13. Sukumar, N., Moran, B., Belytschko, T.: The natural element method in solid mechanics. Int. J. Numer. Meth. Eng. **43**, 839–887 (1998)
14. Liu, W.K., Jun, S., Zhang, Y.F.: Reproducing kernel particle methods. Int. J. Numer. Meth. Eng. **20**, 1081–1106 (1995)
15. Aluru, N.R: A point collocation method based on reproducing kernel approximations. Int. J. Numer. Meth. Eng. **47**, 1083–1121 (2000)
16. Atluri, S.N., Zhu, T.L.: A new meshless local Petrov-0Galerkin (MLPG) approach in computational mechanics. Comput. Mech. **22**, 117–27 (1998)
17. Zhang, X., Yao, Z.H., Zhang, Z.F.: Application of MLPG in large deformation analysis. Acta Mech. Sin. **22**, 331–340 (2006)
18. Liu G., R., Zhang, G.Y., Dai, K.Y.: A linearly conforming point interpolant method (LC-PIM) for 2d solid mechanics problems. Int. J. Comput. Methods **2**, 645–665 (2005)
19. Zhang, G.Y., Liu, G.R., Wang, Y.Y., Han, X. et al.: A linearly conforming point interpolation method (LC-PIM) for three-dimensional elasticity problems. Int. J. Numer. Meth. Eng. **72**, 1524–1543 (2007)
20. Zhou, J.X., Wen, J.B., Zhang, H.Y., Zhang, L.: A nodal integration and post-processing technique based on Voronoi diagram for Galerkin meshless methods. Comput. Methods Appl. Mech. Eng. **192**, 3831–3843 (2003)
21. Dolbow, J., Belytschko, T.: Numerical integration of the Galerkin weak form in meshfree methods. Comput. Mech. **23**, 219–230 (1999)
22. Atluri, S.N., Sladek, J., Sladek, V., Zhu, T.: The local boundary integral equation (LBIE) and its meshless implementation for linear elasticity. Comput. Mech. **25**, 180–198 (2000)
23. Beissel, S., Belytschko, T.: Nodal integration of the element-free Galerkin method. Comput. Methods Appl. Mech. Eng. **139**, 49–74 (1996)
24. Chen, J.S., Wu, C.T., Yoon, S., You, Y.: A stabilized conforming nodal integration for Galerkin mesh-free methods. Int. J. Numer. Meth. Eng. **50**, 435–466 (2001)
25. Dai, K.Y., Liu, G.R., Han, X., Li, Y.: Inelastic analysis of 2D solids using a weak-form RPIM based on deformation theory. Comput. Methods Appl. Mech. Eng. **195**, 4179–4193 (2006)
26. Hsieh, H.H., Tai, W.K.: A simple GPU-based approach for 3D Voronoi diagram construction and visualization. Sim. Modell. Pract. Theory **13**, 681–692 (2005)
27. Li, Q.Y.: Numerical analysis, 3rd edn. Tsinghua University Press, (2001)
28. Zhang, X.: Meshless method, 1rd edn. Tsinghua University Press (2004)